Journal of Materials Chemistry A

PAPER

View Article Online
View Journal | View Issue

Cite this: J. Mater. Chem. A, 2016, 4, 568

Self-assembly of mesoporous $ZnCo_2O_4$ nanomaterials: density functional theory calculation and flexible all-solid-state energy storage†

Deyang Zhang,[a] Yihe Zhang,*[a] Xiaowei Li,[a] Yongsong Luo,[b] Hongwei Huang,[a] Jiaping wang[c] and Paul K. Chu[d]

Received 7th September 2015
Accepted 23rd November 2015

DOI: 10.1039/c5ta07105d

www.rsc.org/MaterialsA

Ternary spinel metal oxide $ZnCo_2O_4$ with Co^{2+} at the tetrahedral sites (8a) in the spinel Co_3O_4 replaced by Zn^{2+} is promising in energy storage and an economical way to fabricate low-toxicity nanostructured $ZnCo_2O_4$ is described. Theoretical calculation confirms the rationality of the experimental scheme and elucidates the underlying reason for the increased band gap. The high electrochemical activity and excellent stability of the $ZnCo_2O_4$ NFs//$ZnCo_2O_4$ NW symmetrical device suggest large potential for energy storage applications. The fabricated device boasts a capacity of 220.6 F g^{-1} at a current density of 2 A g^{-1} and long-term cycling stability with 67.5% of the capacitance retained after 8000 cycles. The maximum energy density of 60.04 W h kg^{-1} at a power density of 1.4 kW kg^{-1} and a power density of 7 kW kg^{-1} at an energy density of 23.72 W h kg^{-1} are achieved at an operating voltage of 1.4 V. This combined experimental and theoretical study provides insights into the design and controllable preparation of nanomaterials for energy storage applications.

1. Introduction

On the heels of the fast development of light and flexible portable electronic devices, such as rollup displays, smart electronic devices, and wearable devices, research on efficient flexible energy storage and conversion devices is becoming very important. In addition, the fast-growing market for hybrid vehicles requires further improvement of the power and energy density of energy storage devices.[1–11] Supercapacitors (SCs) as one of the promising energy storage devices have attracted considerable attention due to their high power density, fast recharge ability, good rate performance, and long life time.[12–19] Previous studies demonstrate that the type and structure of electrode materials determine the performance of SCs. Although carbon continues to be the dominant electrode material in commercial SCs, these devices cannot meet the stringent requirements for future large-scale applications[1,20–22]. Accordingly, much effort has been made to identify better materials, for instance, transition metal oxides, conducting polymers, and hybrid composites, to obtain better specific capacitance and cycle performance.[23–29]

Studies on binary metal oxides (MOs) like Co_3O_4 show that the materials possess high capacitance and excellent cycle life but there are also disadvantages such as low conductivity, toxic cobalt and high cost thereby impeding adoption in high-performance energy storage devices.[20,30] To improve the conductivity, Co_3O_4 can be incorporated with conductive materials such as carbon nanotubes, graphene, carbon fibers, or other carbon-based materials. For example, Yu *et al.*[31] have produced a scrolled structure of Co_3O_4/r-GO by a two-step surfactant-assisted method. The Co_3O_4/r-GO exhibits a large specific capacitance of 163.8 F g^{-1} at a current density of 1 A g^{-1}, which is about 13 times larger than that of pure Co_3O_4. Zhang *et al.*[32] have used an electrodeposition method to fabricate free-standing Co_3O_4 nanosheet arrays on carbon fiber paper without a polymer binder and the materials show enhanced specific capacity and cycling performance. Another method is to replace the metal ions in the binary MO partially to form a ternary *iso*-structure by incorporating compatible metals such as Zn, Cu, Mg, and Fe. This process reduces the cost and toxicity while the electrochemical performance is not affected significantly.

[a]Beijing Key Laboratory of Materials Utilization of Nonmetallic Minerals and Solid Wastes, National Laboratory of Mineral Materials, School of Materials Science and Technology, China University of Geosciences, Beijing, 100083, P. R. China. E-mail: zyh@cugb.edu.cn

[b]School of Physics and Electronic Engineering, Xinyang Normal University, Xinyang 464000, P. R. China

[c]Department of Physics and Tsinghua-Foxconn Nanotechnology Research Center, Tsinghua University, Beijing 100084, China

[d]Department of Physics & Materials Science, City University of Hong Kong, Tat Chee Avenue, Kowloon, Hong Kong, China

† Electronic supplementary information (ESI) available. See DOI: 10.1039/c5ta07105d

Ternary spinel metal oxide $ZnCo_2O_4$ with Co^{2+} at the tetrahedral sites (8a) in the spinel Co_3O_4 replaced by Zn^{2+} (Fig. 1) poses a cost-effective, scalable, and environmentally friendly material suitable for energy storage.[30] Shen *et al.*[33] have fabricated hierarchical $ZnCo_2O_4$ nanorods on nickel foam by a scalable solution approach and they deliver good electrochemical performance in SCs including high specific capacitance (~1400 F g^{-1} at 1 A g^{-1}), excellent rate capability (72.5% capacity retention at 20 A g^{-1}), and good cycling stability (only 3% loss after 1000 cycles at 6 A g^{-1}). Luo *et al.*[34] have employed a cost-effective and simple strategy to prepare a hierarchical $ZnCo_2O_4$@MnO_2 nanocomposite on Ni foam and the unique structure has specific capacitances of 2339 and 1526 F g^{-1} at current densities of 1 and 10 A g^{-1}, respectively, besides a long-term capacity retention of 95.9% after 3000 cycles at 2 A g^{-1} and 94.5% after 8000 cycles at 10 A g^{-1}. However, in spite of recent advances, the devices still fall short in meeting the ever-increasing demands of the modern electronics and hybrid vehicle industry.

In this work, mesoporous $ZnCo_2O_4$ nanomaterials with high electrical conductivity were produced on a flexible substrate. The cost and toxicity of the materials are reduced by substituting Co^{2+} with Zn^{2+} at the tetrahedral sites (8a) in the spinel Co_3O_4. The high electrical conductivity and flexible substrate improve the flexibility, mechanical resilience, volume change, weight, and environmental friendliness[35,36] thereby enabling convenient roll-to-roll processing[37] and fabrication of collapsible and portable SCs.

To evaluate the rationality of the experimental scheme, first-principles calculation based on the density functional theory (DFT) was employed and the electronic structures of Co_3O_4 and $ZnCo_2O_4$ were investigated. In our view, the DFT employed here is badly needed as the calculation results could guide us to design a more reasonable experimental plan and to the best of our knowledge, no similar reports have been found. This combined experimental and theoretical study provides insights into the design and controllable preparation of nanomaterials for energy storage applications.

2. Experimental section

Synthesis of $ZnCo_2O_4$ nanoflowers ($ZnCo_2O_4$ NFs) on nickel-plated metal fibers and $ZnCo_2O_4$ nanowires ($ZnCo_2O_4$ NWs) on carbon fibers

The $ZnCo_2O_4$ NFs were fabricated by a simple hydrothermal method. The nickel-plated metal fibers with dimensions of 1.5 cm × 4 cm were cleaned with 6 M HCl ultrasonically for 30 min to remove the NiO surface layer and then rinsed with deionized (DI) water. In the typical procedure, 1.5 mmol $Zn(NO_3)_2 \cdot 6H_2O$, 3 mmol $Co(NO_3)_2 \cdot 6H_2O$, 2 mmol fluoride NH_4F and 6 mmol $CO(NH_2)_2$ were dissolved in 40 ml of DI water and stirred for 30 min. The solution and the cleaned nickel plated metal fibers were transferred to a 50 ml Teflon-lined stainless steel autoclave which was heated to 130 °C for 5 h. After the autoclave was cooled to ambient temperature, the samples were removed, washed with distilled water, and dried at 60 °C. Afterwards, the samples were annealed at 400 °C in air for 3 h to obtain the $ZnCo_2O_4$ NFs. The $ZnCo_2O_4$ NWs were prepared similarly except that the substrate was changed to carbon fibers.

Materials characterization

The structure and phase of the products were determined by X-ray diffraction (XRD) performed on a D8 Advance (Germany, Bruker) automated X-ray diffractometer system with CuK_α (λ = 1.5406 Å) radiation at 40 kV and 40 mA between 10° and 80° at room temperature. The chemical composition was determined by X-ray photoelectron spectroscopy (XPS, PHI 5600 XPS system). Scanning electron microscopy (SEM) was performed on a HITACHI S-4800 microscope (Japan). Transmission electron

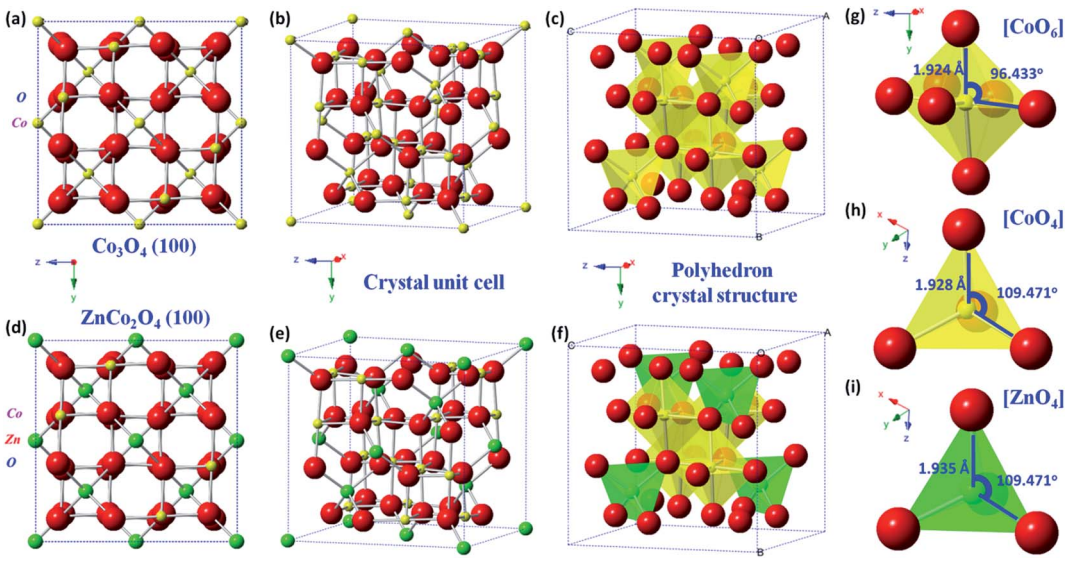

Fig. 1 (a–c) Crystal structure of spinel Co_3O_4; (d–f) crystal structure of spinel $ZnCo_2O_4$; (g–i) CoO_6 octahedron, CoO_4 tetrahedron, and ZnO_4 tetrahedron. Zn ions occupy the tetrahedral sites and Co ions occupy the octahedral sites.

microscopy (TEM) was carried out on a JEOL JEM-2010 in the bright field mode and a HR-TEM JEM-2010FEF at 200 kV. The Raman scattering spectra were acquired on a WITEC CRM200 equipped with a 532 nm laser source and a 50× objective lens. The nitrogen adsorption–desorption isotherms of the samples were measured by using a ASAP 2020 porosimeter at 77 K, and the specific surface area and mesopore size distribution were calculated using the BET and BJH methods.

Electrochemical measurement based on three-electrode supercapacitor testing configuration

The electrochemical tests were conducted on a CHI 660E electrochemical workstation (CH Instruments Inc., Shanghai) with a typical three-electrode cell with the as-prepared sample as the working electrode, Pt foil as the counter electrode, Ag/AgCl electrode as the reference electrode, and 2 M KOH as the electrolyte. Cyclic voltammetry (CV) tests were performed between 0 and 0.8 V at various scan rates ranging from 2 to 50 mV s^{-1} at room temperature. The galvanostatic charge/discharge tests were conducted between 0 and 0.8 V at various current densities between 2–10 A g^{-1}. The electrochemical impedance spectroscopy (EIS) measurements were performed by applying an alternating current voltage with 5 mV amplitude in the frequency range from 0.01 Hz to 100 kHz at the open circuit potential.

Electrochemical measurements of the all-solid-state supercapacitor device

The electrochemical measurements were conducted on a CHI 660E electrochemical workstation (CH Instruments Inc., Shanghai). To fabricate the symmetrical SC prototype, a two-electrode device consisting of $ZnCo_2O_4$ NFs and $ZnCo_2O_4$ NWs as the electrodes was set up. The PVA/KOH gel electrolyte was prepared by adding 2.0 g of PVA and 2.0 g of KOH to 30 ml of H_2O. The mixture was stirred at 80 °C until the solution became clear. Two pieces of the electrodes were immersed in the PVA/KOH solution for 2 min, taken out, and assembled leaving aside the bare carbon and nickel-plated metal fibers as the electrodes. After solidification at room temperature, the symmetrical capacitor was prepared. The experiments were conducted at room temperature. The specific capacitance (F g^{-1}) and current density (A g^{-1}) were calculated from the total mass of the active materials. Cyclic voltammetry (CV) was performed at a scanning rate of 5–100 mV s^{-1} from 0 to 1.4 V at room temperature and the galvanostatic charging–discharging measurements were performed from 0 to 1.4 V at current densities between 2 and 10 A g^{-1}.

First-principles calculation

To calculate the electronic structures of Co_3O_4 and $ZnCo_2O_4$, first-principles calculations were carried out with the spin-polarized Generalized Gradient Approximation (GGA) by adopting the Perdew–Burke–Ernzerhof (PBE) exchange-correlation parameterization to the Density Functional Theory (DFT) incorporating the LDA + U formalism using the CASTEP program.[38] A plane-wave basis with a kinetic energy cutoff of 400.0 eV and a Monkhorst-Pack grid with a 4 × 4 × 4 *k*-point mesh for the integration in the Brillouin zone were used, and the value of the smearing was 0.2 eV. The electronic minimization parameter of the total energy/atom convergence tolerance was 5.0×10^{-6} eV.

3. Results and discussion

Fig. 2 shows the DFT results of the spinel $ZnCo_2O_4$. Fig. 2a ($ZnCo_2O_4$) and S1a† (Co_3O_4) show that the band gap of Co_3O_4 increases slightly from 1.357 eV to 1.663 eV when Zn^{2+} replaces Co^{2+}. From the literature it was found that the experimental value of Co_3O_4 ≈ 1.5–1.6 eV,[39] and the calculated band gap energy of the Co_3O_4 are 1.1026 (ref. 40) and 1.8 eV,[41] respectively. Our result (1.357 eV) is in good agreement with the experimental value. Fig. 2d (blue and yellow regions indicate electron increase and decrease, respectively) explains the reason for the increased band gap. The electron accepting ability of Zn^{2+} is weaker than that of Co^{2+} and Zn^{2+} at the tetrahedral sites (8a) in the spinel structure weakens the electron accepting ability of $ZnCo_2O_4$. This is further confirmed by the corresponding densities of states (DOS). The total DOS revealed that the spinel Co_3O_4 (Fig. S1b†) has less DOS near the Fermi level than the spinel $ZnCo_2O_4$ (Fig. 2b). According to quantum theory, only electrons near the Fermi level can contribute to the current under an external electric field and the electrical conductivity is proportional to the electrons at the Fermi level.[42] The electron effective masses of Co_3O_4 and $ZnCo_2O_4$ were compared by a simple method. Fig. S2† shows the band structures of the two materials, and it is found that the energy bands of $ZnCo_2O_4$ are more flat than that of Co_3O_4 near the Fermi level. This means that the former has a larger electron effective mass, and further illustrates the $ZnCo_2O_4$ has lower band mobility compared with Co_3O_4. Hence, the conductivity of $ZnCo_2O_4$ is slightly less than that of Co_3O_4 as a result of the change in the band structure. The electrical resistivity of Co_3O_4 and $ZnCo_2O_4$ was also measured by a four-point probe method. The square resistance of Co_3O_4 is 52 kΩ sq^{-1} and the thickness is about 0.2 mm, so the electrical resistivity of the Co_3O_4 is about 1040 Ω cm, which is in good agreement with the previous report.[43] Under the same experimental conditions, the electrical resistivity of $ZnCo_2O_4$ is an order of magnitude higher than that of Co_3O_4. However, in practice, a small change is tolerable if benefits such as eco-friendliness (low toxicity) and low cost are considered. These satisfactory results evaluated the rationality of the experimental scheme. The calculation also indicates that the magnetic properties of the spinel structure disappear after Zn^{2+} substitutes Co^{2+}.

The X-ray diffraction (XRD) pattern in Fig. 3a that can be indexed to the cubic spinel structure of $ZnCo_2O_4$ (JCPDS no. 23-1390)[44] shows the dominant (311) peaks revealing the preferred (311) orientation. The characteristic peaks of laser Raman spectrograms in Fig. 3b and XPS spectra in Fig. 3c–f disclose the presence of Zn, Co and O suggesting the formation of $ZnCo_2O_4$.

Fig. 4d and 5d schematically illustrate the formation mechanism of $ZnCo_2O_4$ nanoflowers ($ZnCo_2O_4$ NFs) and $ZnCo_2O_4$ nanowires ($ZnCo_2O_4$ NWs), respectively. Nickel plated metal

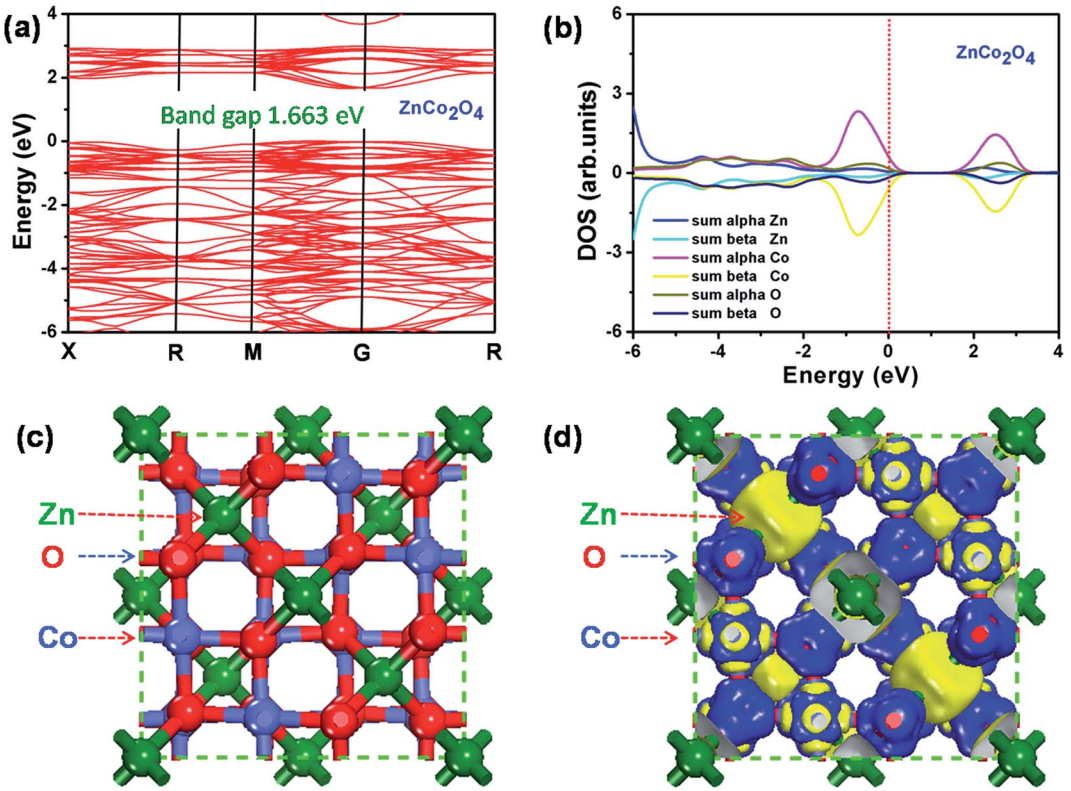

Fig. 2 (a) Calculated band structure; (b) Total densities of states; (d) electron density difference by the CASTEP for the spinel $ZnCo_2O_4$ (the blue and yellow regions indicate electron increase and decrease, respectively). (c) (1 0 0) crystal face of spinel $ZnCo_2O_4$.

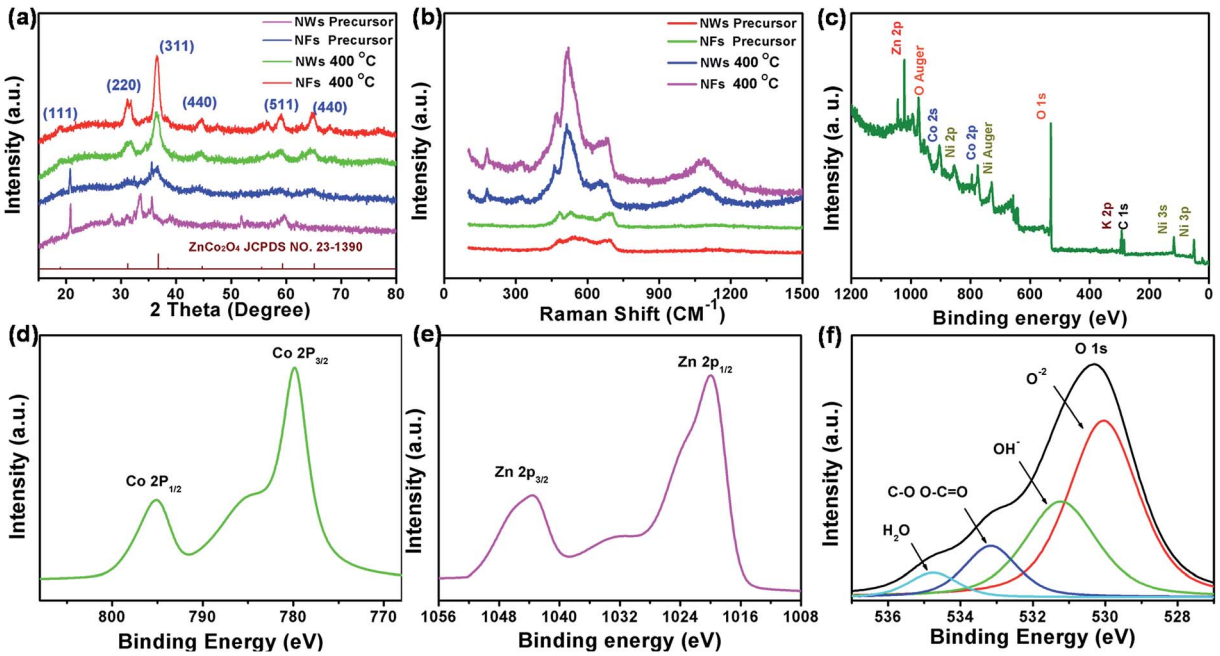

Fig. 3 Properties of the as-prepared spinel $ZnCo_2O_4$ nanomaterials. (a) XRD patterns of $ZnCo_2O_4$ NFs and NWs; (b) Raman spectra of $ZnCo_2O_4$ NFs and NWs; (c) XPS general spectrum of spinel $ZnCo_2O_4$; (d–f) corresponding Co 2p, Zn 2p, and O 1s XPS peaks.

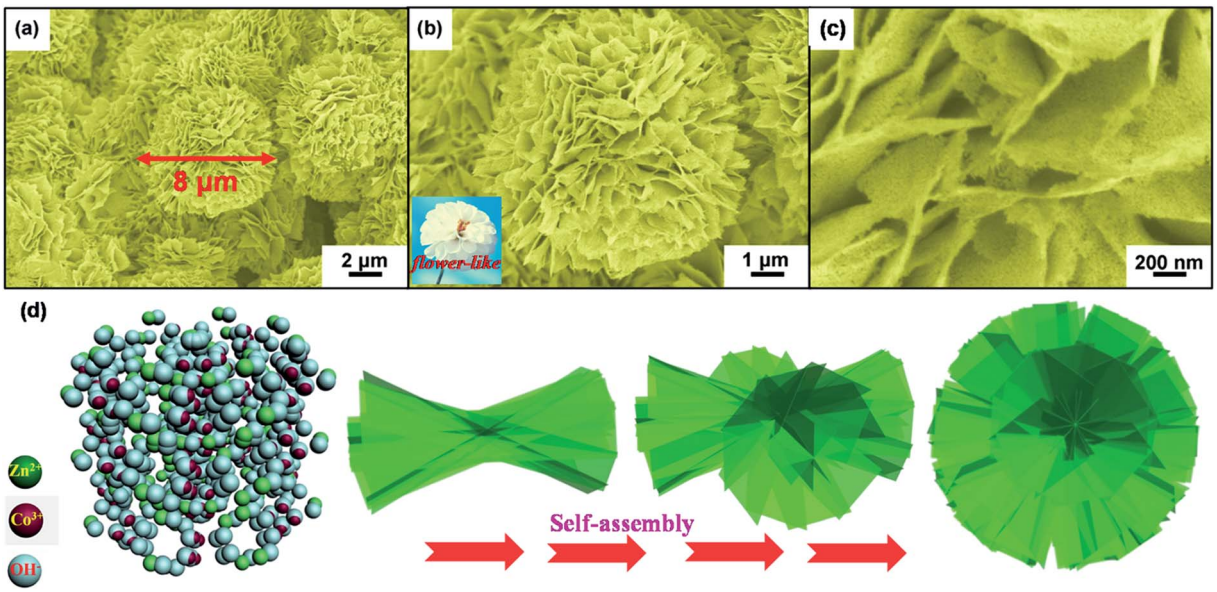

Fig. 4 Morphologies and the schematic diagram for the formation mechanism of the 3D $ZnCo_2O_4$ NFs. (a, and b) low-magnification and enlarged SEM images of $ZnCo_2O_4$ NFs; (c) high-magnification SEM image of $ZnCo_2O_4$ NFs; (d) the proposed mechanism for the fabrication of $ZnCo_2O_4$ NFs by the self-assembly process.

fibers and carbon fibers are flexible and conductive rendering them excellent substrates to fabricate nanostructured $ZnCo_2O_4$ hydrothermally according to the following reactions (1–4):[45]

$$H_2NCONH_2 + H_2O \rightarrow 2NH_3 + CO_2 \quad (1)$$

$$CO_2 + H_2O \rightarrow CO_3^{2-} + 2H^+ \quad (2)$$

$$NH_3 + H_2O \rightarrow NH_4^+ + OH^- \quad (3)$$

$$2/3Co^{2+} + 1/3Zn^{2+} + OH^- + 1/2CO_3^{2-} + nH_2O \rightarrow Zn_{1/3}Co_{2/3}(OH)(CO_3)_{1/2}nH_2O \quad (4)$$

Annealing at 400 °C (ramping rate of 2 °C min^{-1}) converts the precursors into spinel $ZnCo_2O_4$ NFs and $ZnCo_2O_4$ NWs as follows:

$$6Zn_{1/3}Co_{2/3}(OH)(CO_3)_{1/2}nH_2O + O_2 \rightarrow 2ZnCo_2O_4 + 3CO_2\uparrow + (6n + 3)H_2O \quad (5)$$

The formation involves two steps. First, the $ZnCo_2O_4$ NF and $ZnCo_2O_4$ NW precursors self-assemble under hydrothermal conditions. At the suitable pH controlled by the mass of urea and hydrolysis producing OH^- and CO_3^{2-} at a high temperature

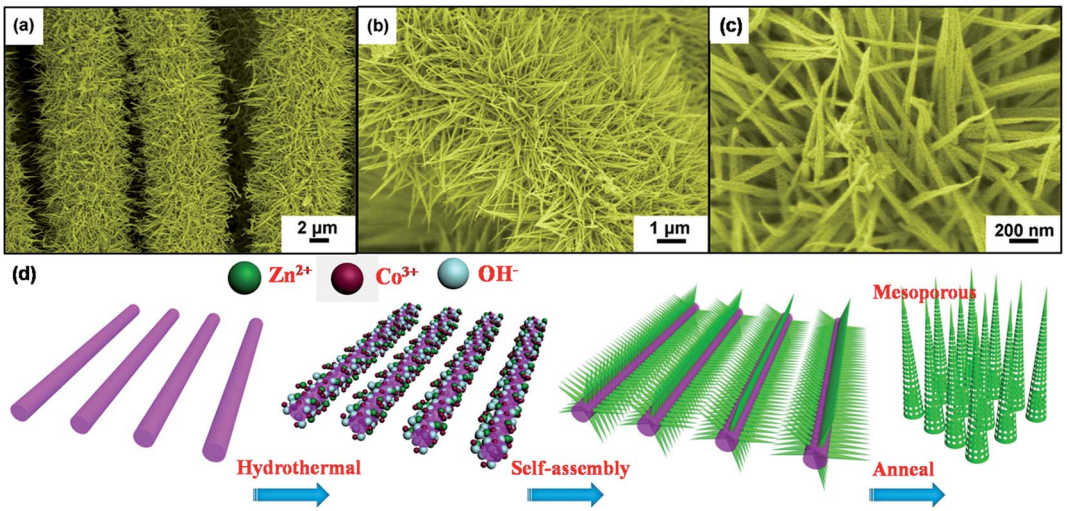

Fig. 5 Morphologies and the schematic diagram for the formation mechanism of the $ZnCo_2O_4$ NW arrays. (a, and b) low-magnification and enlarged SEM images of $ZnCo_2O_4$ NWs; (c) high-magnification SEM image of $ZnCo_2O_4$ NWs; (d) the proposed mechanism for the fabrication of $ZnCo_2O_4$ NW arrays by the self-assembly process.

and high pressure, Zn^{2+} and Co^{2+} combine with OH^- and CO_3^{2-} in the solution and post-annealing in air to form $ZnCo_2O_4$ NFs and $ZnCo_2O_4$ NWs on the substrate.

SEM images disclose that $ZnCo_2O_4$ NFs and $ZnCo_2O_4$ NWs are produced in high yields. The optical images of the $ZnCo_2O_4$ NFs and $ZnCo_2O_4$ NWs are depicted in Fig. S3† and the color contrast indicates that the materials were fabricated successfully. Fig. S4† presents the SEM images of the conductive and flexible substrates, nickel plated metal fibers (Fig. S4a and b†) and carbon fibers (Fig. S4c and d†). The surface of the carbon fibers is smooth prior to the $ZnCo_2O_4$ NW growth and the particles on the metal fibers maybe generated by nickel plating. Fig. 4a–c display the SEM images of $ZnCo_2O_4$ NFs at low, medium and high magnifications with an average diameter of 8 μm (Fig. 4a). Fig. S5† shows large areas of the flower-like $ZnCo_2O_4$. The higher-magnification SEM image in Fig. 4c shows that the $ZnCo_2O_4$ NFs are composed of many nanosheets which consist of a large number of nanoparticles. These nanosheets are interconnected and grow radially from the center forming a flower-like structure. This unique morphology improves the electron transport between the nanosheets and improves the durability of the structure during the fast redox reaction. Undoubtedly, these advantages may enhance the electrochemical performance. Fig. 5a–c depict the SEM images of the $ZnCo_2O_4$ NWs at different magnifications indicating that the as-prepared nanowire array growth on the carbon fibers occurred on a large area and was uniform. Fig. 5a and b disclose retention of the 3D structure of the carbon fibers which are covered by $ZnCo_2O_4$ NWs uniformly. The examination of an individual carbon fiber reveals that the $ZnCo_2O_4$ NWs grow orderly and closely on the carbon fibers with a large aspect ratio (Fig. 5c). After ultrasonic treatment for several minutes, the $ZnCo_2O_4$ NWs are examined by FE-SEM which shows that the nanowires adhere well on the carbon fibers. The high-magnification SEM images in Fig. 4c and 5c show that the $ZnCo_2O_4$ NFs and $ZnCo_2O_4$ NWs have porous structures due to gas release during decomposition of the precursors. The Brunauer–Emmett–Teller (BET) surface area of $ZnCo_2O_4$ NWs was calculated to be 59.386 $m^2\ g^{-1}$, and the average pore width is about 50 nm. The large surface area is expected to yield a high specific capacitance due to the easy access of the active materials to the interface in the redox process. The TEM images of the $ZnCo_2O_4$ NFs and $ZnCo_2O_4$ NWs in Fig. 6 confirm that the porous structure consists of many nanoparticles. The lattice spacing of 0.24 nm shown in Fig. 6b and e corresponds to the (311) planes of spinel $ZnCo_2O_4$ and the circular SAED patterns of the $ZnCo_2O_4$ NFs (inset in Fig. 6b) and $ZnCo_2O_4$ NWs (inset of Fig. 6e) indicate a polycrystalline nature.

To evaluate the electrochemical performance of the synthesized nanostructures, electrochemical measurements were performed using a three-electrode system with 2 M KOH aqueous electrolyte, a platinum foil counter electrode and an Ag/AgCl reference electrode. The CV curves of $ZnCo_2O_4$ NF and $ZnCo_2O_4$ NW electrodes at various scan rates with a potential window ranging from 0 to 0.8 V (*vs.* Ag/AgCl) are presented in Fig. 7a and d. The shapes of these CV curves remained virtually unchanged with the potential scan rates varied from 2 to 50 mV s^{-1}, revealing the ideal capacitive behaviors and good rate capabilities of the $ZnCo_2O_4$ NF and $ZnCo_2O_4$ NW electrodes. The shape of the CV curves clearly reveals the pseudocapacitive characteristics. Specifically, a pair of redox peaks can be observed within the potential range from 0 to 0.8 V (*vs.* Ag/AgCl) for all sweep rates, which is mainly related to the faradic redox reactions in the alkaline electrolyte. With the increase of scan rate, the cathodic peak position shifts to a lower potential, which is attributed to the polarization effect. Fig. 7b and e illustrate the galvanostatic charge–discharge (GCD) curves of $ZnCo_2O_4$ NF and $ZnCo_2O_4$ NW electrodes measured in the current densities from 2 to 10 A g^{-1}. These charging and discharging curves of the ternary electrodes are highly symmetric, arising from the ideal capacitance behavior and the fast Faraday reaction. Fig. 7c and f schematically illustrate the kinetic advantages of the hybrid structures in electrochemical energy storage. As shown in Fig. 4c, the nanoflowers are composed of many porous nanosheets and these nanosheets are interconnected with each other; not only this unique structure improves the electron transport between the nanosheets but also improves the durability of the structure during the fast redox reaction. The analogous one-dimensional porous nanowire structure provides an excellent electronic transmission path in the electrochemical reaction. Moreover, the speed of the electronic transmission was further accelerated due to the flexible and conductive substrates. Without question, these advantages could enhance the electrochemical performance.

To further explore the practical applications of this design, an all-solid-state symmetric SC was assembled using $ZnCo_2O_4$ NFs and $ZnCo_2O_4$ NWs as the electrodes with polyvinyl alcohol (PVA)/KOH as the gel electrolyte (denoted as $ZnCo_2O_4$ NFs// $ZnCo_2O_4$ NWs). In contrast to liquid-based SCs, solid-state devices have several advantages such as flexibility, ease of fabrication, large working temperature and improved safety. Fig. 8a and b show the photographs of the small and flexible device and Fig. 8c schematically illustrates the structure. The PVA/KOH gel serves as the electrolyte and the separator simultaneously in this device thus simplifying the assembly process. Fig. 8d displays the CV curves of the device at different voltages at a scanning rate of 10 mV s^{-1}. The curves are stable even at 1.4 V indicating good capacitive behavior. Fig. 8e shows the CV curves acquired at scanning rates of 5, 10, 20, 50, and 100 mV s^{-1} in a voltage window of 0 and 1.4 V. The CV profiles are stable as the scanning rate increases from 5 to 100 mV s^{-1} revealing fast charging and discharging characteristics. The GCD curves obtained at different current densities are presented in Fig. 8f. The discharge curves are almost symmetrical to the charge curves, indicating good capacitive behavior of the device. The corresponding specific capacitances plotted in Fig. 9a were derived by using the following equation:

$$C = (I \times \Delta t)/(m \times \Delta V) \quad (6)$$

where I (A) is the constant discharge current and m (g), Δt (s), and ΔV (V) designate the mass of active materials, discharging time, and potential drop during discharging, respectively. The total mass of active materials is approximately 20 mg. The

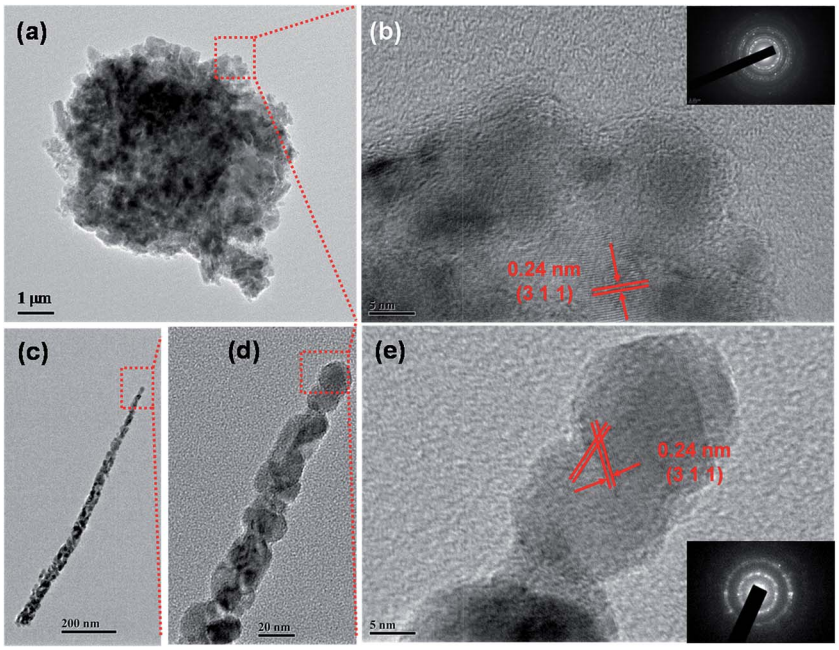

Fig. 6 (a, and b) Low-magnification and high-magnification TEM images of the $ZnCo_2O_4$ NFs; (c–e) low-magnification and high-magnification TEM images of the $ZnCo_2O_4$ NWs. The insets of (b) and (e) are the corresponding SAED patterns obtained from the $ZnCo_2O_4$ NFs and $ZnCo_2O_4$ NWs.

device shows capacitances of 220.6, 167.6, 148, 116.6 and 87.14 F g^{-1} at current densities of 2, 3, 4, 6, and 10 A g^{-1}, respectively. Fig. 9b shows the cycling performance at a current density of 2 A g^{-1} for up to 8000 cycles and a retention of 67.5%. The degradation in the capacitance stems from the destruction of the electrode by the harsh redox reactions and the consumption of the gel electrolyte caused by an irreversible reaction between the electrode material and electrolyte. As illustrated in the inset

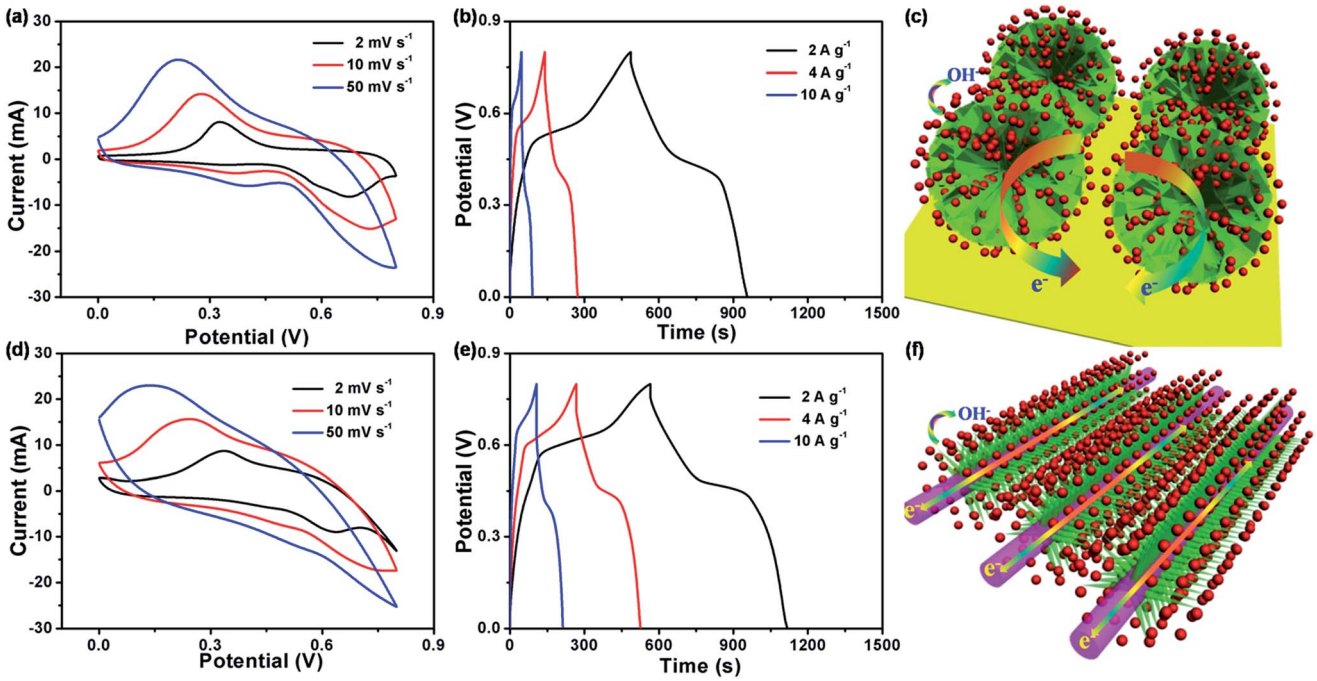

Fig. 7 Electrochemical properties of the $ZnCo_2O_4$ nanomaterials under a three-electrode measurement system. (a) and (d) CV curves of the $ZnCo_2O_4$ NFs and $ZnCo_2O_4$ NWs at different scan rates; (b) and (e) discharging curves of the $ZnCo_2O_4$ NFs and $ZnCo_2O_4$ NWs at different current densities; (c) and (f) schematic diagrams showing the kinetic advantages of the $ZnCo_2O_4$ NFs and $ZnCo_2O_4$ NWs in electrochemical energy storage.

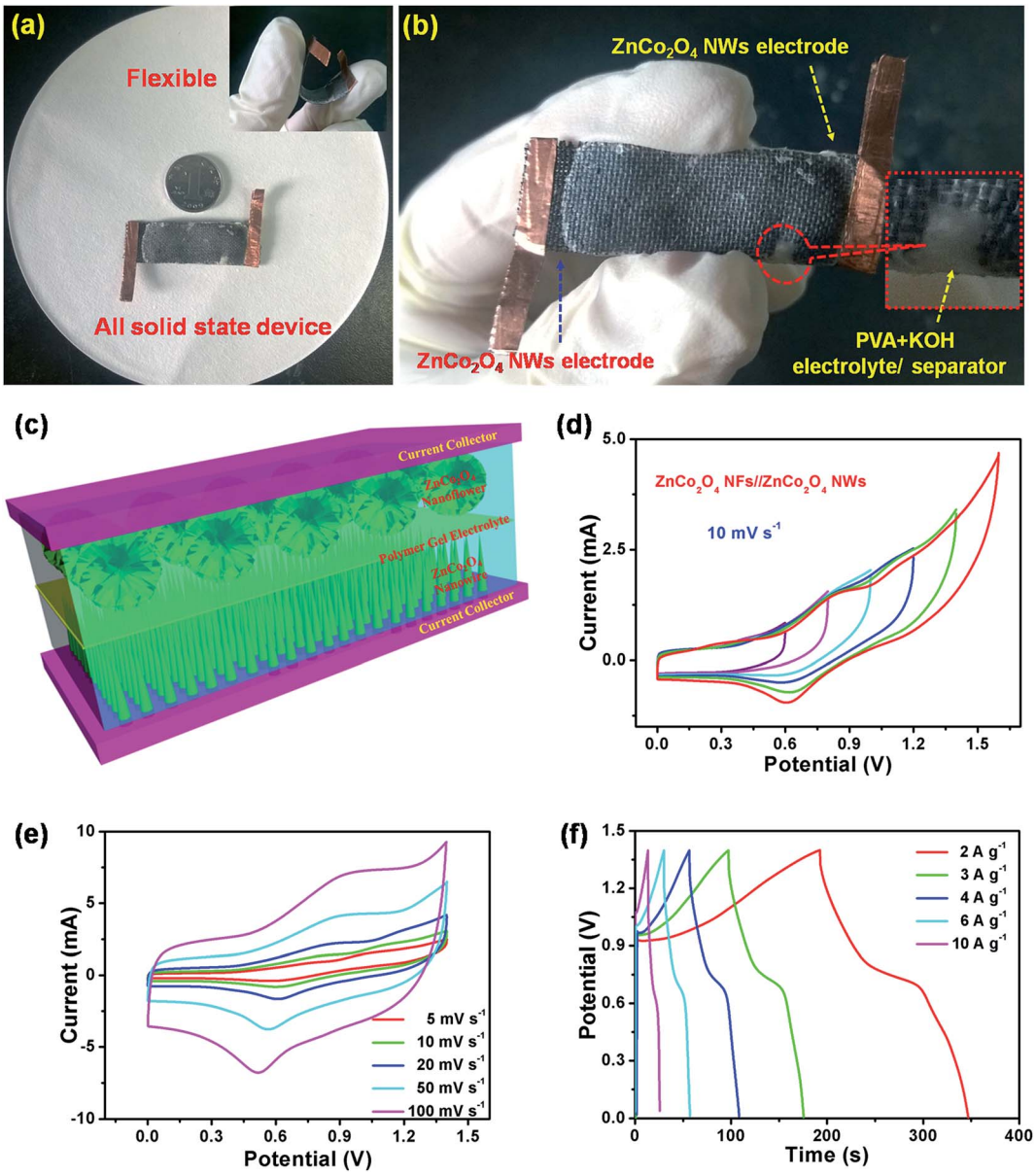

Fig. 8 (a, and b) Photographs of the device; (c) schematic illustration of the structure of the all-solid-state device; (d) CV curves acquired at different voltages at a scanning rate of 10 mV s^{-1}; (e) CV curves measured at scanning rates of 5, 10, 20, 50, and 100 mV s^{-1} at voltages between 0 and 1.4 V; (f) GCD curves of the device at different current densities.

of Fig. 9b, the $ZnCo_2O_4$ NF and $ZnCo_2O_4$ NW structures were well maintained and overall preserved with little structural deformation after 8000 cycles. The intrinsic electrochemical and kinetic mechanisms of the electrodes were analyzed by the EIS studies. Fig. 9c illustrates the Nyquist plots of EIS spectra of $ZnCo_2O_4$ NFs, $ZnCo_2O_4$ NWs and the device in the frequency range from 10 kHz to 0.01 Hz. In the low-frequency area, the inclined line represents the Warburg (W) impedance corresponding to the electrolyte diffusion in porous electrodes and proton diffusion in host materials. The $ZnCo_2O_4$ NW electrode has the largest slope of all electrodes, indicating its best capacitive performance with lower diffusion resistance. This can be attributed to the fact that nanowires are separate from each other, which facilitates the flow of the electrolyte. In the high frequency area, the intercept to the x axis represents the bulk resistance of the electrochemical system (R_e), and the semicircle corresponds to the parallel combination of double-layer capacitance (CPE) and charge transfer resistance (R_{ct}) at the working electrode–electrolyte interface. Compared to the other electrodes, $ZnCo_2O_4$ NW electrode has a smaller R_e, since the carbon fiber substrate increases the electrical conductivity.

To evaluate the flexibility and stability of the device, the circulation properties are assessed at different bending angles of 0 (without bending), 60, 90, and 120°. The influence of the bending-induced mechanical stress on the specific capacitance is illustrated in Fig. 9d which shows a negligible capacitance change even though the device is bent substantially. The Ragone plot describing the relationship between the energy and

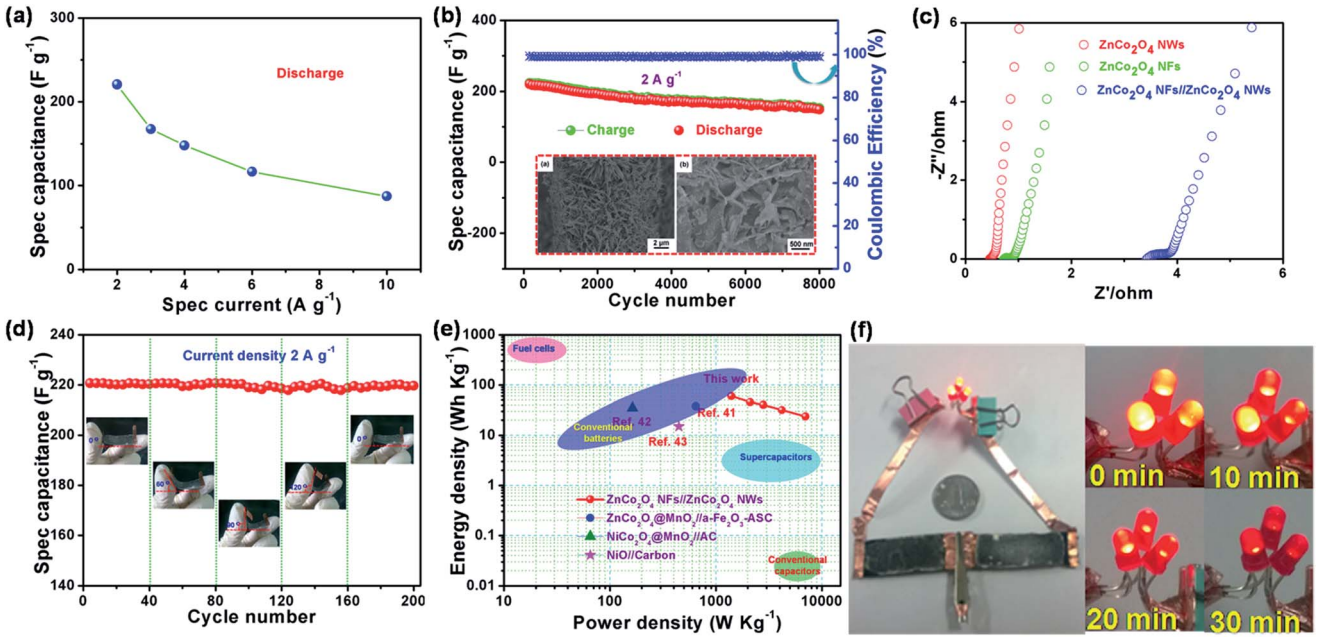

Fig. 9 (a) Calculated specific capacities; (b) cycling performance of the device at a current density of 2 A g^{-1} for 8000 cycles; (c) electrochemical impedance spectra (EIS) of the $ZnCo_2O_4$ NW, $ZnCo_2O_4$ NF and $ZnCo_2O_4$ NFs//$ZnCo_2O_4$ NW electrodes; (d) influence of the bending-induced mechanical stress upon specific capacitance; (e) Ragone plots of the device in comparison with other recently reported values for SCs; (f) optical images of three red LEDs powered by two all solid-state SCs connected in series.

power densities is shown in Fig. 9e with data obtained from traditional lithium ion batteries (LIBs) and EDLC provided for comparison. The energy and power densities (E and P) are calculated by using the following equations:

$$E = (C \times \Delta V^2)/2 \quad (7)$$

$$P = E/\Delta t \quad (8)$$

where C (F g^{-1}) is the specific capacitance of the device. The maximum energy density of 60.04 W h kg^{-1} at a power density of 1.4 kW kg^{-1} and a power density of 7 kW kg^{-1} at an energy density of 23.72 W h kg^{-1} are achieved at an operating voltage of 1.4 V, which are better than the energy and power densities achieved previously from $ZnCo_2O_4$@MnO_2//a-Fe_2O_3 (energy density 37.8 W h kg^{-1} at a power density of 648 W kg^{-1}),[46] $NiCo_2O_4$@MnO_2//AC (energy density 35 W h kg^{-1} at a power density of 163 W kg^{-1}),[47] and NiO//carbon (15 W h kg^{-1} at a power density of 447 W kg^{-1}).[48]

In order to explore the potential applications of $ZnCo_2O_4$ NF//$ZnCo_2O_4$ NW device as a flexible power source, we further demonstrate the practical application of the device by powering a light-emitting diode (LED). As shown in the insets in Fig. 9f, the two devices connected in series can power three 3 mm diameter red LEDs [1.8 V, 20 mA] for more than 10 min (strong light) and they are effective even for 30 min.

4. Conclusion

A low-cost and large-area technique to produce eco-friendly $ZnCo_2O_4$ NFs and $ZnCo_2O_4$ NWs is designed and described. The high electrochemical activity and stability of the $ZnCo_2O_4$ NFs// $ZnCo_2O_4$ NW symmetrical device suggest the large potential of $ZnCo_2O_4$ in energy storage. Theoretical assessment confirms the rationality of the experimental scheme and explains the increased band gap. The device shows a superior capacity of 220.6 F g^{-1} at a current density of 2 A g^{-1} as well as long-term cycling stability with 67.5% capacitance retention after 8000 cycles. The maximum energy density of 60.04 W h kg^{-1} at a power density of 1.4 kW kg^{-1} and a power density of 7 kW kg^{-1} at an energy density of 23.72 W h kg^{-1} are accomplished at an operating voltage of 1.4 V. The excellent properties, stability, and durability bode well for commercial adoption of the nanostructured $ZnCo_2O_4$ materials in future high-performance SCs.

Acknowledgements

This work was jointly supported by the Fundamental Research Funds for the Central Universities (53200959770), Special Construction project of Beijing city Education Committee (519002650733), and City University of Hong Kong Applied Research Grant (ARG) No. 9667104.

Notes and references

1 P. Simon and Y. Gogotsi, *Nat. Mater.*, 2008, 7, 845–854.
2 M. S. Dresselhaus and I. L. Thomas, *Nature*, 2011, **414**, 332–337.
3 D. Y. Zhang, Y. H. Zhang, Y. S. Luo and P. K. Chu, *Nano Energy*, 2015, **13**, 45–47.

4 Y. S. Luo, J. S. Luo, J. Jiang, W. W. Zhou, H. P. Yang, X. Y. Qi, H. Zhang, H. J. Fan, Y. W. Y. Denis, C. M. Li and T. Yu, *Energy Environ. Sci.*, 2012, **5**, 6559–6566.
5 Z. Y. Zhang, F. Xiao, L. H. Qian, J. W. Xiao, S. Wang and Y. Q. Liu, *Adv. Energy Mater.*, 2014, **4**, 1400064–1400073.
6 W. M. Du, X. Han, L. Lin, M. X. Chen, X. Y. Li, C. F. Pan and Z. L. Wang, *Adv. Energy Mater.*, 2014, **4**, 1301592–1301797.
7 C. F. Pan, L. Dong, G. Zhu, S. Niu, R. M. Yu, Q. Yang, Y. Liu and Z. L. Wang, *Nat. Photonics*, 2013, **7**, 752–758.
8 Z. N. Yu, M. McInnis, J. Calderon, S. Seal and J. Thomas, *Nano Energy*, 2015, **11**, 611–620.
9 D. Y. Zhang, H. L. Yan, Y. Lu, K. W. Qiu, C. L. Wang, Y. H. Zhang, X. M. Liu, J. S. Luo and Y. S. Luo, *Dalton Trans.*, 2014, **43**, 15887–15897.
10 D. Y. Zhang, H. L. Yan, Y. Lu, K. W. Qiu, C. L. Wang, C. C. Tang, Y. H. Zhang, C. W. Cheng and Y. S. Luo, *Nanoscale Res. Lett.*, 2013, **9**, 139–147.
11 Y. P. Fu, X. Cai, H. W. Wu, Z. B. Lv, S. C. Hou, M. Peng, X. Yu and D. C. Zou, *Adv. Mater.*, 2012, **24**, 5713–5718.
12 Z. N. Yu, L. Tetard, L. Zhai and J. Thomas, *Energy Environ. Sci.*, 2015, **8**, 702–730.
13 F. Meng and Y. Ding, *Adv. Mater.*, 2011, **23**, 4098–4102.
14 K. Wang, W. Zou, B. Quan, A. Yu, H. Wu, P. Jiang and Z. Wei, *Adv. Energy Mater.*, 2011, **1**, 1068.
15 M. Kaempgen, C. K. Chan, J. Ma, Y. Cui and G. Gruner, *Nano Lett.*, 2009, **9**, 1872–1876.
16 A. S. Arico, P. Bruce, B. Scrosati, J. M. Tarascon and W. V. Schalkwijk, *Nat. Mater.*, 2005, **4**, 366–377.
17 P. Simon, Y. Gogotsi and B. Dunn, *Science Magazine*, 2014, **343**, 1210–1211.
18 Z. N. Yu and J. Thomas, *Adv. Mater.*, 2014, **26**, 4279–4285.
19 H. Y. Wang, F. X. Xiao, L. Yu, B. Liu and X. W. David Lou, *Small*, 2014, **10**, 3181–3186.
20 L. F. Shen, Q. Che, H. S. Li and X. G. Zhang, *Adv. Funct.Mater.*, 2014, **24**, 2736.
21 K. Jost, C. R. Perez, J. K. McDonough, V. Presser, M. Heon, G. Dion and Y. Gogotsi, *Energy Environ. Sci.*, 2011, **4**, 5060–5067.
22 M. V. Reddy, G. V. Subba Rao and B. V. R. Chowdari, *Chem. Rev.*, 2013, **113**, 5364–5457.
23 J. P. Liu, J. Jiang, C. W. Cheng, H. X. Li, J. X. Zhang, H. Gong and H. J. Fan, *Adv. Mater.*, 2011, **23**, 2076–2081.
24 Y. S. Luo, J. Jiang, W. W. Zhou, H. P. Yang, J. S. Luo, X. Y. Qi, H. Zhang, D. Y. W. Yu, C. M. Li and T. Yu, *J. Mater. Chem.*, 2012, **22**, 8634–8640.
25 L. F. Hu, L. M. Wu, M. Y. Liao, X. H. Hu, X. S. Fang, L. Hu, L. Wu and M. Liao, *Adv. Funct. Mater.*, 2012, **22**, 998–1004.
26 Y. S. Luo, J. S. Luo, W. W. Zhou, X. Y. Qi, H. Zhang, Y. W. Y. Denis, C. M. Li, H. J. Fan and T. Yu, *J. Mater. Chem. A*, 2013, **1**, 273–281.
27 C. Zhou, Y. W. Zhang, Y. Y. Li and J. P. Liu, *Nano Lett.*, 2013, **13**, 2078–2085.
28 J. S. Luo, X. H. Xia, Y. S. Luo, C. Guan, J. L. Liu, X. Y. Qi, C. F. Ng, T. Yu, H. Zhang and H. J. Fan, *Adv. Energy Mater.*, 2013, **3**, 737–743.
29 J. S. Luo, J. L. Liu, Z. Y. Zeng, C. F. Ng, L. J. Ma, H. Zhang, J. Y. Lin, Z. X. Shen and H. J. Fan, *Nano Lett.*, 2013, **13**, 6136–6143.
30 W. Luo, X. L. Hu, Y. M. Sun and Y. H. Huang, *J. Mater. Chem.*, 2012, **22**, 8916–8921.
31 W. W. Zhou, J. P. Liu, T. Chen, K. S. Tan, X. T. Jia, Z. Q. Luo, C. X. Cong, H. P. Yang, C. M. Li and T. Yu, *Phys. Chem. Chem. Phys.*, 2011, **13**, 14462–14465.
32 Q. C. Liu, J. J. Xu, Z. W. Chang and X. B. Zhang, *J. Mater. Chem. A*, 2014, **2**, 6081–6085.
33 B. Liu, B. Y. Liu, Q. F. Wang, X. F. Wang, Q. Y. Xiang, D. Chen and G. Z. Shen, *ACS Appl. Mater. Interfaces*, 2013, **5**, 10011–10017.
34 K. W. Qiu, Y. Lu, D. Y. Zhang, J. B. Cheng, H. L. Yan, J. Y. Xu, X. M. Liu, J. K. Kim and Y. S. Luo, *Nano Energy*, 2015, **11**, 687–696.
35 A. C. Siegel, S. T. Phillips, M. D. Dickey, N. Lu, Z. Suo and G. M. Whitesides, *Adv. Funct. Mater.*, 2010, **20**, 28–35.
36 A. W. Martinez, S. T. Phillips, M. J. Butte and G. M. Whitesides, *Angew. Chem., Int. Ed.*, 2007, **46**, 1318–1320.
37 F. C. Krebs, T. Tromholt and M. Jorgensen, *Nanoscale*, 2010, **2**, 873–886.
38 S. J. Clark, M. D. Segall, C. J. Pickard, P. J. Hasnip, M. J. Probert, K. Refson and M. C. Payne, *Zeitschrift für Kristallographie*, 2005, **220**, 567–570.
39 J. van Elp, J. L. Wieland, H. Eskes, P. Kuiper, G. A. Sawatzky, F. M. F. de Groot and T. S. Turner, *Phys. Rev. B: Condens. Matter Mater. Phys.*, 1991, **44**, 6090–6103.
40 Y. R. Zhu, X. B. Ji, Z. P. Wu, W. X. Song, H. S. Hou, Z. B. Wu, X. He, Q. Y. Chen and C. E. Banks, *J. Power Sources*, 2014, **267**, 888–900.
41 Y. C. Wang, T. Zhou, K. Jiang, P. M. Da, Z. Peng, J. Tang, B. Kong, W. B. Cai, Z. Q. Yang and G. F. Zheng, *Adv. Energy Mater.*, DOI: 10.1002/aenm.201400696.
42 U. Mizutani, *Introduction to the Electron Theory of Metals*, Cambridge University Press, United Kingdom, 2001.
43 V. R. Shinde, S. B. Mahadik, T. P. Gujar and C. D. Lokhande, *Appl. Surf. Sci.*, 2006, **252**, 7487–7492.
44 N. C. Li, C. R. Martin and B. Scrosati, *J. Power Sources*, 2001, **97**, 240–243.
45 H. X. Chen, Q. B. Zhang, J. X. Wang, Q. Wang, X. Zhou, X. H. Li, Y. Yang and K. L. Zhang, *Nano Energy*, 2014, **10**, 245–258.
46 W. Q. Ma, H. H. Nan, Z. X. Gu, B. Y. Geng and X. J. Zhang, *J. Mater. Chem., A*, 2015, **3**, 5442–5448.
47 Z. S. Wu, W. C. Ren, D. W. Wang, F. Li, B. L. Liu and H. M. Cheng, *ACS Nano*, 2010, **4**, 5835–5842.
48 X. Lu, M. Yu, T. Zhai, G. Wang, S. Xie, T. Liu, C. Liang, Y. Tong and Y. Li, *Nano Lett.*, 2013, **13**, 2628–2633.